JGR Atmospheres

RESEARCH ARTICLE
10.1029/2021JD036295

The Contribution of Convection to the Stratospheric Water Vapor: The First Budget Using a Global Storm-Resolving Model

Thibaut Dauhut[1] and **Cathy Hohenegger**[1]

[1]Max Planck Institute for Meteorology, Hamburg, Germany

Key Points:

- The global water vapor budget of the low stratosphere is computed for the first time using a Global Storm-Resolving Model (GSRM)
- ICOsahedral Non-hydrostatic GSRM simulates the global distribution of very deep convection and its hydration of the stratosphere
- Over the simulated period, very deep convective systems contribute to 11% of the stratospheric water vapor input

Supporting Information:

Supporting Information may be found in the online version of this article.

Correspondence to:

T. Dauhut,
thibaut.dauhut@mpimet.mpg.de

Citation:

Dauhut, T., & Hohenegger, C. (2022). The contribution of convection to the stratospheric water vapor: The first budget using a global storm-resolving model. *Journal of Geophysical Research: Atmospheres*, *127*, e2021JD036295. https://doi.org/10.1029/2021JD036295

Received 1 DEC 2021
Accepted 9 FEB 2022

Abstract The deepest convection on Earth injects water in the tropical stratosphere, but its contribution to the global stratospheric water budget remains uncertain. The Global Storm-Resolving Model ICOsahedral Non-hydrostatic is used to simulate the moistening of the lower stratosphere for 40 days during boreal summer. The decomposition of the water vapor budget in the tropical lower stratosphere (TLS, 10°S–30°N, and 17–20 km altitude) indicates that the average moistening (+21 Tg) over the simulated 40-day period is the result of the combined effect of the vertical water vapor transport from the troposphere (+27 Tg), microphysical phase changes and subgrid-scale transport (+2 Tg), partly compensated by horizontal water vapor export (−8 Tg). The very deep convective systems, explicitly represented thanks to the employed 2.5 km grid spacing of the model, are identified using the very low Outgoing Longwave Radiation of their cold cloud tops. The water vapor budget reveals that the vertical transport, the sublimation and the subgrid-scale transport at their top contribute together to 11% of the water vapor mass input into the TLS.

1. Introduction

Stratospheric water vapor plays an important role for climate as its variations can significantly increase or offset global warming (Forster & Shine, 2002; Shindell, 2001; Solomon et al., 2010). Water vapor actually impacts both the radiative and chemical properties of the stratosphere, being both a strong greenhouse gas (Stevens, 2013) and a precursor of ozone depleting substances (Stenke & Grewe, 2005). In mid- to upper-stratosphere, the main origin of water vapor is the oxidation of methane (Brasseur & Solomon, 2006). Below, in low-to mid-stratosphere, the main source of water vapor is the upward transport from the troposphere. These air masses and their water content are then redistributed upward and poleward by the Brewer-Dobson circulation. Stratospheric water vapor is expected to increase with global warming, mostly because of enhanced transport from the troposphere (Revell et al., 2016). This provides a positive feedback on global warming that increases climate sensitivity (Banerjee et al., 2019; Dessler et al., 2013). As the processes that dominantly control the transport of water vapor between the troposphere and the stratosphere may change with global warming, it is key to quantify the magnitude of the processes involved in this transport.

The transport of water by injection of tropospheric air into the stratosphere occurs via two different pathways. They are both taking place at the same time but with very contrasted spatial and temporal scales (Randel & Jensen, 2013). On the one hand, water vapor is transported into the stratosphere by the tropical upwelling due to the Brewer-Dobson circulation. This process is slow but occurs at the scale of the tropics (e.g., Fueglistaler et al., 2009). The concentration of water vapor in the air that enters the stratosphere in this way is low (typically about 4 ppmv). At the tropopause, several processes, namely transitional cooling by waves, homogeneous condensation, deposition and sedimentation, lead to freeze-drying, that is, to the condensation of water vapor in excess, reducing the actual amount of water vapor entering the stratosphere (e.g., E. Jensen & Pfister, 2004; E. J. Jensen et al., 2013). On the other hand, the direct transport of ice particles into the stratosphere by very deep convective systems, that is, systems that overshoot the tropopause, allows water molecules to bypass the tropopause cold point thanks to their transport in the ice phase. This is followed by sublimation in the sub-saturated stratosphere, which moistens the stratosphere (Corti et al., 2008; Dauhut et al., 2018; Khaykin et al., 2009; X. M. Liu et al., 2010; Smith, 2021). This pathway is fast, locally intense, but occurs infrequently and at the scale of the convective systems.

Quantifying the contribution of convection to the global stratospheric water vapor budget is particularly challenging because of the range of involved scales between the small-scale convective transport and the global effect

to quantify. Only three studies from two groups provided such estimates so far, two for boreal winter (Schoeberl et al., 2014, 2018) and one for the full year (Dauhut et al., 2015). Two studies from another group provided estimates for two 7-day periods in both boreal summer and winter, but only in the vicinity of the tropical cold-point tropopause at the 100 hPa level (Ueyama et al., 2015, 2018). Summarizing the results of these studies, Schoeberl et al. (2014) found a 13% contribution of convection, by applying a Lagrangian model that follows air mass trajectories to reanalysis and comparing the results with and without the effect of convection. In their study, the effect of convection is deduced indirectly from the resulting adjustment of the water vapor content of the air masses in the presence of cloud along the trajectory. Such a quantification is limited by the accuracy and the resolution of the cloud height dataset as well as of the wind and temperature fields used to advect the air masses. Using the same method, Schoeberl et al. (2018) revised their estimate using an updated and more correct temperature dataset, with colder tropopause, and found a convective contribution of 2% only. Using also a Lagrangian model but with a more sophisticated, computationally expensive microphysical scheme, Ueyama et al. (2015) and Ueyama et al. (2018) found a 14% and 15% contribution of convection to the water vapor content at 100 hPa for their two 7-day periods in boreal winter and summer, respectively. The level at which their investigation is focused is located close, though slightly below the averaged cold-point tropopause. The impact of convection on the full stratospheric water vapor budget might be larger than these estimates for two main reasons: first the air masses are very close to saturation at the cold-point, limiting the hydration by convection, second they can be hydrated by convection at higher altitudes, during their whole rise through the low stratosphere. Dauhut et al. (2015) found an 18% contribution by simulating one very deep convective system with a Large-Eddy Simulation (LES) and upscaling the subsequent stratosphere hydration to the whole tropics. Here the estimate relies on the ability of the LES model to represent the hydration, on the representativeness of the study case and on the estimated frequency of very deep convective systems in the tropics, which varies with season. It should be kept in mind that such studies are highly dependent on the chosen representation of the microphysics. Large uncertainty remains in quantifying the importance of convection for the global stratospheric water budget.

Here, to take up the challenge we use a distinct approach. We take advantage of a GSRM that is able to both represent the convective-scale processes explicitly and simulate those over the full globe. The global atmosphere is simulated with the ICOsahedral Non-hydrostatic model (ICON), integrated with a grid spacing of 2.5 km during 40 days in the framework of the DYAMOND intercomparison project (Stevens et al., 2019). The convection is resolved and the vertical resolution around the tropopause, about 600 m, is fine enough to capture the small-scale mixing at the top of the overshoot and the subsequent shallow hydration patches that form above the tropical tropopause, as will be shown. Taking advantage of these two aspects, we derive for the first time a global budget of the low-stratospheric water vapor using a model that resolves convection, and provide a new estimate of the convective contribution.

In Section 2 the observational data sets, the simulation and the analysis methods are presented. Section 3 describes the observed stratospheric humidity field and assesses the ability of our model to represent this field and its variations. Section 4 presents the budget of the stratospheric water vapor to identify the origin of its temporal variations. Section 5 quantifies the contribution of the very deep convective systems to this stratospheric water budget. Section 6 discusses the implications of our investigation, trying in particular to reconcile the various estimates of the convective contribution to the stratospheric water vapor as deduced from various observations and modeling studies. Section 7 gives the conclusions.

2. Data and Methods

2.1. MLS Observations

To assess the representation of the stratospheric water vapor field and its variations in the simulation, we use the observations (version v4.22) from the Microwave Limb Sounder (MLS) instrument onboard of the NASA's Earth Observing System Aura satellite (Waters et al., 2006). Microwave Limb Sounder has a daily near global coverage thanks to its near-polar orbit. We use the gridded water vapor product on the seven pressure levels located between 100 and 132 hPa, between 1 August and 9 September 2016 to match the simulation time period, as well as in eight other years to document the year-to-year variability. The vertical resolution ranges between 3.0 and 3.2 km, and the horizontal resolution between profiles ranges between 190 and 265 km. The zonal and temporal averaging of the MLS observations reduces much of the uncertainty resulting from the precision of the instrument, but the uncertainty due to its accuracy is unchanged and ranges from 4% to 9% (Livesey et al., 2017).

The recommendations for data screening given in Livesey et al. (2017) are followed. We do not apply the MLS averaging kernels to the simulated stratospheric water vapor. As shown by the study of Ploeger et al. (2013), using the averaging kernels only matters for the estimated stratospheric water vapor content at high latitudes. As our study is focusing on the tropics, using the averaging kernel is not necessary.

2.2. CERES Observations

The development of the very deep convective systems, characterized by their extremely cold cloud tops, can be monitored using spatial observations of the Outgoing Longwave Radiation (OLR). Here we use the observations from the CERES project (Clouds and the Earth's Radiant Energy System; Wielicki et al., 1996) as given in the CERES SYN1deg Edition4A product (Doelling et al., 2016). The latter is a global dataset with a resolution of 1°. It contains, among others variables, hourly averaged OLR. The radiances are measured by the MODIS imager onboard of the Terra and Aqua satellites, with daily global coverage. To account for local, hourly variations of OLR, measurements from new-generation geostationary satellite imagers are incorporated. The resolution of the CERES dataset is too coarse to capture individual overshoots, that have a width of about 10 km and a lifetime of 15 min (Dauhut et al., 2018), but the cold temperature of the anvil tops and of the rising or collapsing overshoots leaves a low-value and large-scale signature in the OLR field that allows us to detect the very deep convective systems. MODIS and geostationary infrared measurements have been extensively used to detect the overshooting tops in the past (e.g., Bedka et al., 2010; Sohn et al., 2009). The CERES product, that combines the two and provides an hourly global coverage is used here to validate the geographical distribution of the deep convective activity in the simulation.

2.3. DYAMOND ICON Simulation

The global troposphere and stratosphere are simulated for 40 days starting on 01 August 2016 with the Eulerian ICON atmospheric model (Icosahedral Nonhydrostatic Weather and Climate Model, Zängl et al., 2015), under the framework of the DYAMOND intercomparison project (DYnamics of the Atmospheric general circulation Modeled On Non-hydrostatic Domains, Stevens et al., 2019). We use here the simulation performed with a horizontal grid spacing of 2.5 km. The vertical grid spacing ranges between 20 m at the surface and 1.8 km at 44 km altitude (top of the physical domain, below the sponge layer), and is about 600 m at the tropopause. The DYAMOND set-up is described in details in Stevens et al. (2019), while the set-up, parameterizations used and validation of this particular ICON simulation are presented in Hohenegger et al. (2020). In short, deep and shallow convection are explicitly represented, without the use of any convection parametrization. Cloud and precipitation are represented by the prognostic specific mass content of five hydrometeor species: cloud water, cloud ice, rain, snow and graupel, whose evolutions are calculated by a bulk one-moment microphysics scheme (Baldauf et al., 2011). The precipitating ice hydrometeors (snow and graupel) are assumed to have a size distribution that is exponentially decaying with particle size, and a fall speed that only depends on particle size. A comparison (not shown) to the size distributions reported by Woods et al. (2018) for Tropical Tropaupose Layer (TTL) cirrus indicates that the number concentrations are in the range of the ones observed between −90°C and −70°C for the large precipitating hydrometeors (larger than 100 μm), whereas they are too low for the smaller hydrometeors. Turbulent fluxes are represented by a turbulent scheme based on a prognostic equation for turbulent kinetic energy (Raschendorfer, 2001). Heating and cooling rates due to radiation are calculated every 15 min with the Rapid Radiative Transfer Model (Mlawer et al., 1997; Mlawer & Clough, 1998). Chemical reactions are not included, this is not an issue since the source of stratospheric water vapor by methane oxidation is active well above the investigated area that stops at 24-km altitude.

The atmosphere as well as soil moisture and temperature are initialized on 1 August 2016 at 00 UTC with the analysis from the European Centre for Medium-Range Weather Forecast (ECMWF), and then evolve freely. Sea surface temperature and sea ice are prescribed from ECMWF operational analysis. In order to account for the spin up of the atmosphere, the first day of the simulation is discarded when computing the water vapor budget described in the following section. As the model is allowed to freely evolve, the simulated fields are expected to differ from the observed ones, especially after 5 days of simulation time when much of the atmospheric predictability is lost. For this reason, in the current study, the simulated fields are not only compared to the observed fields of 2016, but also to those of eight other years (all shown in Supporting Information S1).

As seen in Lee et al. (2019), a grid spacing of 2.5 km allows representing the convective overshoots into the stratosphere and the mixing leading to the local hydration. The results are however sensitive to the chosen grid spacing. Dauhut et al. (2015) analyzed the sensitivity of the transport by one very deep convective system to the horizontal grid spacing, varying it from 100 to 1600 m. They found that the updraft properties (vertical velocity, hydrometeor content) and the stratospheric hydration start to converge at a horizontal grid spacing finer than 200 m, with 20%–25% weaker transport at kilometric horizontal grid spacing. The current study may thus underestimate the hydration of the stratosphere by the convection. Not only the horizontal resolution, but also the vertical resolution, may affect the results. Dauhut et al. (2018) investigated the processes at the overshooting tops and found that the subsequent hydration at each top is determined by its maximal overshooting altitude, using 100-m vertical grid spacing. The 600-m vertical grid spacing used here certainly undersamples the full range of overshooting depths, although it is not clear whether this will lead to a high or low bias on the estimated convective hydration.

The output of the simulation, provided at a 3-hourly frequency, is initially on a native grid made of triangular cells. In order to apply the budget decomposition described below, we first regridded the data on a Cartesian, latitude-longitude grid, that has a grid spacing of 0.1°.

2.4. Water Vapor Budget

To investigate the causes of the variations in the water vapor content of the lower stratosphere, we decompose the water vapor budget at each grid cell with the following equation, consistent with the continuity equation used in ICON to achieve mass conservation (Equation 5 in Zängl et al., 2015):

$$\frac{\partial \rho q}{\partial t} = \left(-\frac{\partial u \rho q}{\partial x} - \frac{\partial v \rho q}{\partial y} \right) - \frac{\partial w \rho q}{\partial z} + s \tag{1}$$

where ρ is the full air density, q is the specific humidity, u, v, and w are the zonal, meridional and vertical components of the wind, respectively, and s is the sink/source term due to microphysics (sublimation, condensation, deposition) and subgrid-scale transport (turbulent fluxes and coherent flows that are finer than 0.1°, the resolution of the analysis). The first two terms in brackets on the right-hand side denote the horizontal convergence of the moisture flux, and the third one is the vertical convergence of the moisture flux, all simulated by the explicit flow on the 0.1° analysis grid. The sink/source term is computed as a residue. With such a decomposition of the water vapor budget, the variations of water vapor mass in each grid cell equals the convergence of the fluxes across the edges, plus a sink/source term that must be understood as the local variations not accounted for by the explicit flow at 0.1°. This decomposition is consistent with the equation solved in the Eulerian ICON model, and differs from the equation of conservation formulated this way: $\frac{D\rho q}{Dt} = s_{Lag}$ where s_{Lag} is the water vapor sink/source term associated to a followed air parcel, and $\frac{D\rho q}{Dt} = \frac{\partial \rho q}{\partial t} + u.\frac{\partial \rho q}{\partial x} + v.\frac{\partial \rho q}{\partial y} + w.\frac{\partial \rho q}{\partial z}$ is the material derivative of water vapor mass. The two decompositions differ by a divergence term, that is non-zero since ICON is fully compressible. We opted for Equation 1 because it is the one used to include the microphysical water vapor variations in ICON (Reinert, 2020). In the whole study, the specific humidity and the integrals of the terms of Equation 1 are systematically converted into volume mixing ratios.

3. Moistening of the Stratosphere

The distributions of the low-stratospheric water vapor in the MLS observations and in the ICON simulation are shown in Figures 1a–1c as zonal and temporal averages over the simulated period. Two years are shown for the MLS observations (2016 and 2017) to illustrate the year-to-year variability and more years can be found in the SI. The simulation correctly reproduces the contrast between the moist region up to 60 hPa in the northern hemisphere and the dry region between 80 and 40 hPa in the southern hemisphere. Except for the latitudes between 15° and 35°S, where the simulation exhibits a moist bias at the tropopause, the simulation produces values in agreement with the MLS observations within 1 ppmv (within 21%). Between 10°S and 30°N and between 90 and 50 hPa, that corresponds to the region of investigation defined below, the ICON moist bias with respect to MLS observation in 2016 (2017) reaches a maximum of +0.45 (+0.25) ppmv, and +0.4 (+0.1) ppmv on average. As a matter of reference, the inter-annual variability of humidity in this region, computed as the standard deviation between the MLS average volume mixing ratio in this region between 2011 and 2019, amounts to 0.25 ppmv.

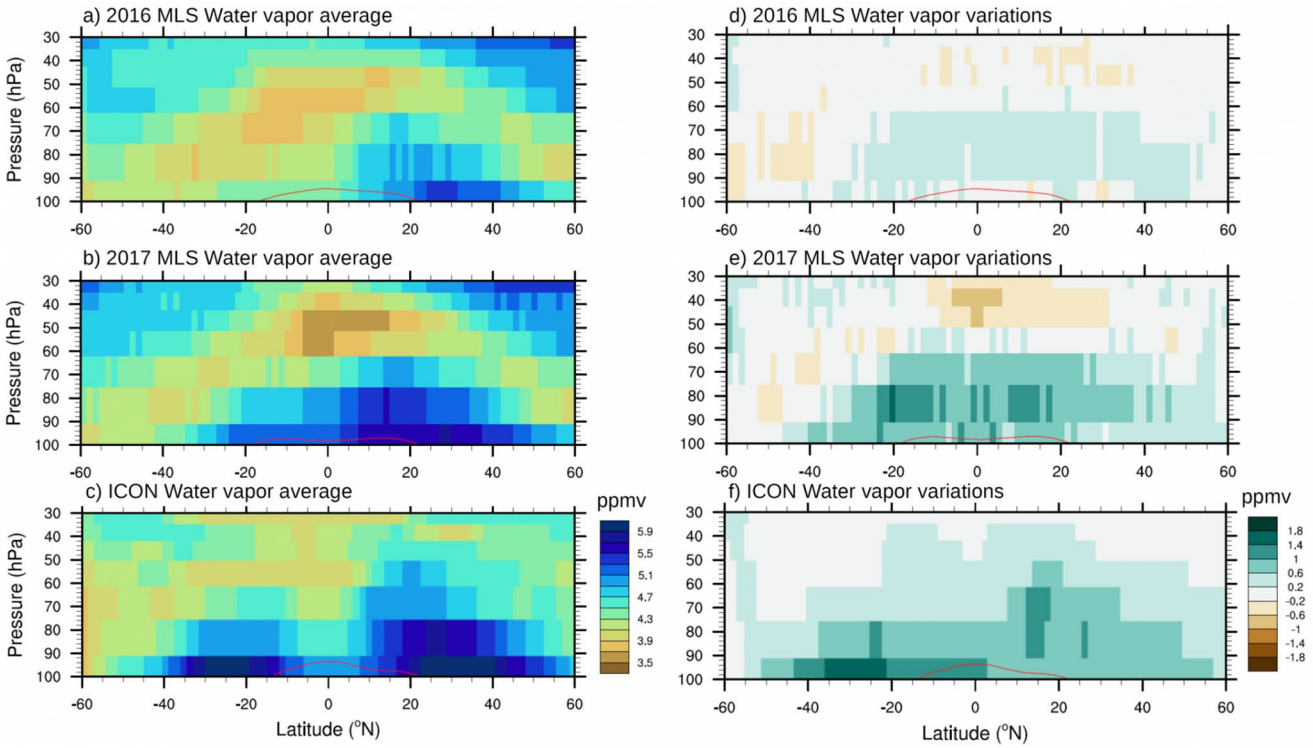

Figure 1. Zonal average of the water vapor volume mixing ratio (a–c) averaged over the period of simulation: 01 August to 09 September, and (d–f) the difference between the average over the last day and over the first day of this period. The latter is titled *water vapor variations* and correspond to the time integral of the first term of Equation 1. (a and d) MLS observations in 2016 (b and e) in 2017, and (c and f) ICON simulation. Note that due to the measurement geometry the MLS data on consecutive pressure levels are not fully independent. The red line is the 380-K isentropic surface, computed from the time and zonal average of the potential temperature fields.

The less-than-0.5-ppmv bias with respect to the MLS observations is also much smaller than the biases generally apparent in traditional global Eulerian models: many state-of-the-art General Circulation Models (GCMs) and Chemistry Climate Models (CCMs) exhibit very large biases, about ±2 ppmv (Eyring et al., 2006; Hardiman et al., 2015). Several factors contribute to these biases, in particular the propagation of incorrect humidity values from the upper troposphere by the vertical advection scheme (Hardiman et al., 2015) and biases in tropical tropopause temperatures (Eyring et al., 2006). A common limitation of GCMs and CCMs is their coarse vertical and horizontal resolutions. Besides inaccuracy in the large scale cross-tropopause transport (Stenke et al., 2008), their representation of convection is not designed to reproduce the overshoot transport up into the stratosphere, as illustrated for one convective parametrization in Dauhut et al. (2018).

In terms of the temporal evolution of the low-stratospheric humidity (Figures 1d–1f), both MLS observations and ICON simulation show an increase between 01 August and 09 September. The observations show for 2016 a moistening of the low stratosphere of 0.2–0.6 ppmv, up to a height of 50 hPa, over latitudes spanning 40°S to 60°N. Such a moistening is part of the annual cycle of the stratospheric water vapor, and can actually be of much larger amplitude in other years, as Figure S2 in Supporting Information S1 shows with up to 1.8 ppmv in 2017 (Figure 1e). A simple bulk computation can explain these variations solely based on a typical upward velocity $w = 4.10^{-4}$ m/s and the water vapor gradients $\frac{\partial q}{\partial z}$ that one can estimate from Figure 1: The moistening Δq equals $-w.\frac{\partial q}{\partial z}.\Delta t$. For instance, in ICON at 10°N, between 62 hPa (4.9 ppmv) and 34 hPa (4.1 ppmv) $\frac{\partial q}{\partial z} \simeq -2.10^{-4}$ ppmv/m. For $\Delta t = 40$ days this leads to $\Delta q = +0.3$ ppmv, consistent with the water vapor variation shown in Figure 1f Above 50 hPa, and south of 40°S, the variation is negative, and is due to the upward and poleward advection of the dry phase of the lower tropical stratosphere by the Brewer-Dobson circulation. Similar bulk computations can explain why the Brewer-Dobson circulation induces less drying in the ICON simulation than in the observations. This is because the ICON initial stratosphere above 40 hPa, and south of 40°S, is slightly drier than in the MLS observations and has then smaller humidity gradients.

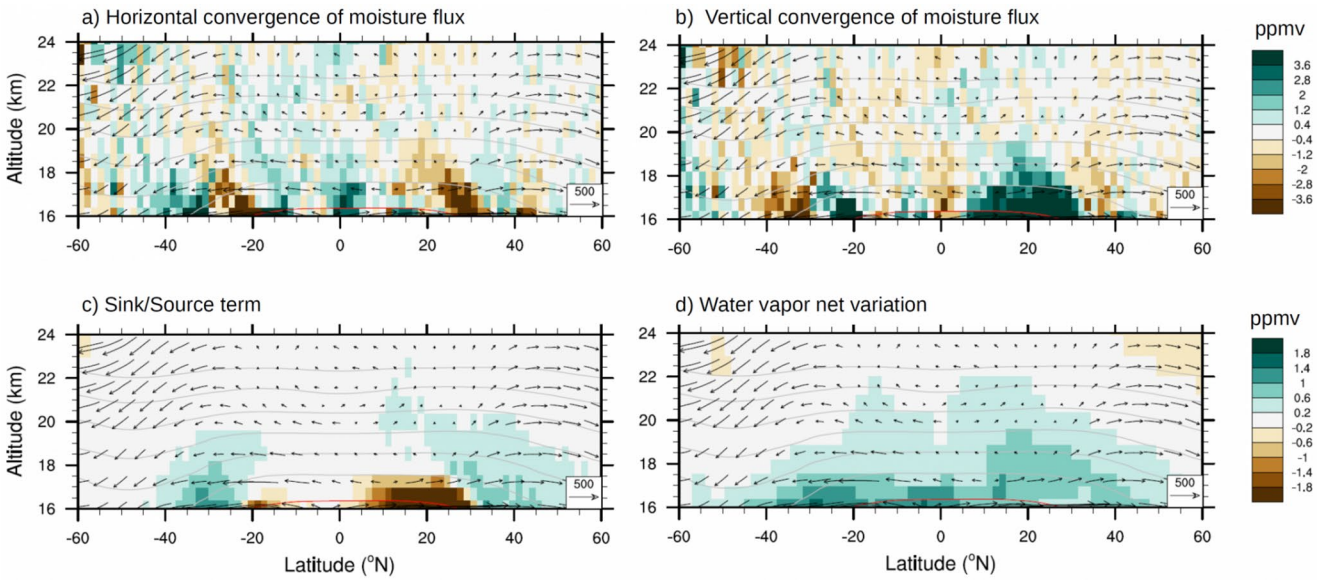

Figure 2. Zonal average of the water vapor budget terms (Equation 1), integrated over the period from 2 August to 8 September included, from the ICON simulation. (a) Horizontal convergence of moisture flux, (b) vertical convergence of moisture flux, (c) sink/source term due to microphysics and subgrid-scale transport, and (d) water vapor net variation. Panels (a–c) share the same color scale (the top one), panel (d) uses the bottom color scale. The fine lines locate the altitude of the isentropic surfaces, computed from the time and zonal average of the potential temperature field, with levels starting from 380 K (the red line) and increasing by steps of 30 K up to 560 K. In all panels the arrows represent the time average of the mean residual meridional and vertical velocities, the unit is m/h for the meridional component and m/day for the vertical component. Different units are used for meridional and vertical components in order to facilitate the visualization.

To quantify the contribution of the tropical convection to this moistening, and more generally to the water vapor input into the stratosphere, our study focuses on a wide latitudinal band, between 10°S and 30°N, that encompasses well the Inter-Tropical Convergence Zone (ITCZ) during the simulated period (cf. Figure 3), where air enters the stratosphere from the troposphere (the head of the atmospheric tape-recorder, Mote, 1995). At these latitudes we define the tropical lower stratosphere (TLS) as the 3-km deep region above the tropopause: between 17 and 20 km altitudes. This region is where the agreement between observations and simulation is best. The altitude range corresponds approximately to the observational pressure levels between 90 and 50 hPa. In this region and over the simulated period, the water vapor mass increase is +29 Tg in the ICON simulation and +12 Tg (+28 Tg) in MLS observations in 2016 (2017) (Figures 1d–1f). The interannual variability of this moistening is very large (Figure S2 in Supporting Information S1), with an average and a standard deviation both equal to 11 Tg over 9 years 2011–2019. The ICON simulation lies in the upper range, typical of observed years like 2017 that exhibits a large TLS moistening between 1 August and 9 September.

The following section investigates the origin of the TLS moistening by decomposing the water vapor budget to shed some light on the contribution by the convergence of the moisture fluxes and by the sink/source term.

4. Origin of the Moistening

The decomposition of the water vapor budget following Equation 1 allows us to quantify the contributions of moisture flux convergence and of the sink/source term to the net variation of the simulated water vapor. The terms of Equation 1 are zonally averaged and integrated over the course of the simulation (Figure 2). The resulting water vapor mass variations per unit volume are converted into volume mixing ratio variations in order to facilitate the comparison with the background values. Mean residual meridional and vertical velocities are overlaid in order to visualize the low-stratospheric circulation, and to assess the strength of the Brewer-Dobson circulation as it drives the large-scale water vapor transport. The distribution of the mean residual vertical velocity at 70 hPa in ICON (near 18.5 km altitude) is in very good agreement with the climatological one in August, as given in Figure 4 of Butchart (2014). The values are upward up to 0.3 mm/s between 20°S and 40°N and downward elsewhere, down to −0.5 mm/s around 50°S.

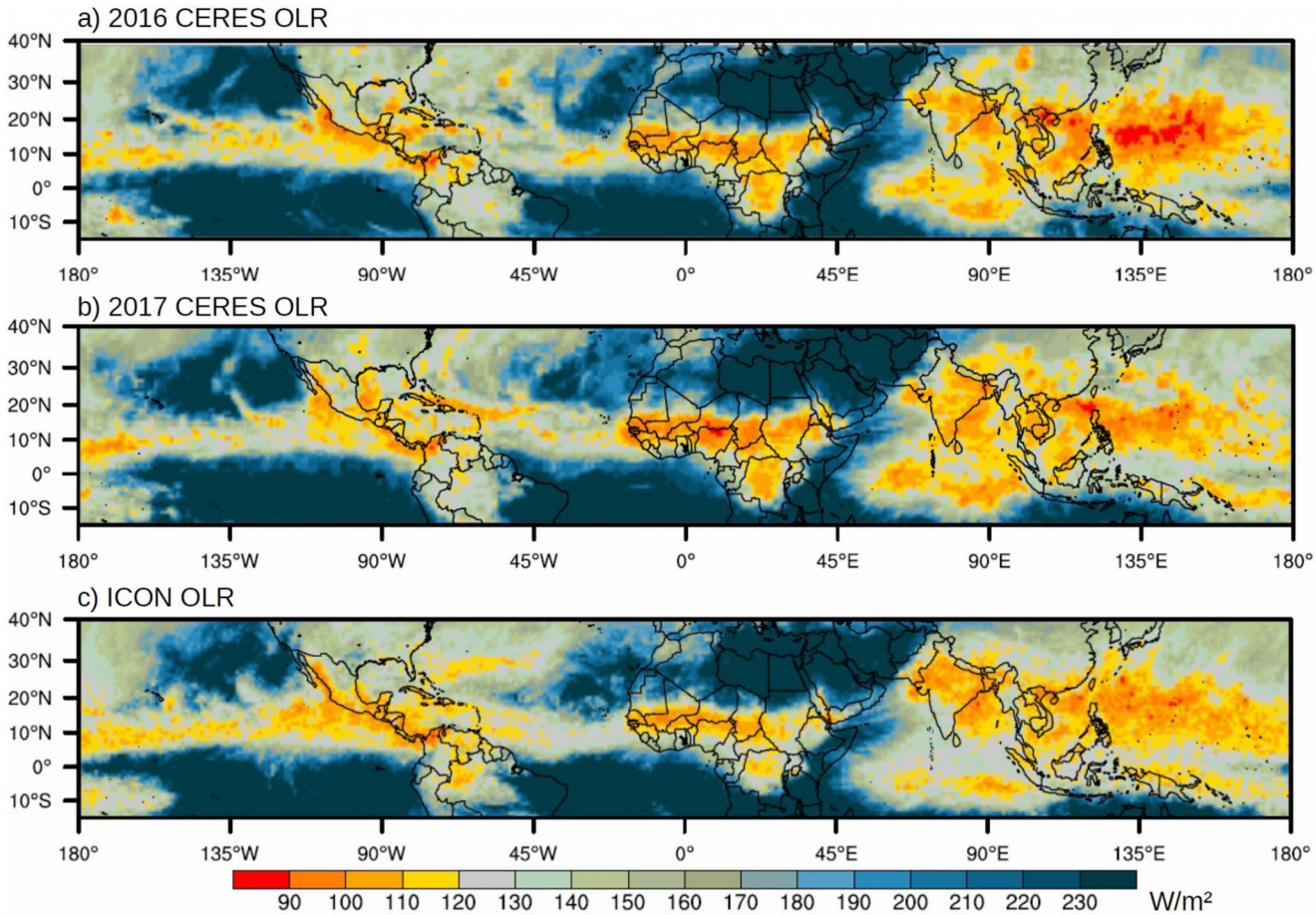

Figure 3. Geographical distribution of the first percentile of the OLR time series at each grid point over the period from 1 August to 9 September in (a) the CERES observations for 2016, (b) for 2017, and (c) the ICON simulation. For each pixel, the value of the first percentile of the OLR time series is represented.

The net variation of water vapor in the lower stratosphere is positive, up to 22 km in the tropics, and maximizes at 16–17 km in the vicinity of the 380-K isentropic surface (Figure 2d). The pattern of the water vapor variation matches well with the result of Figure 1, despite the use of altitude coordinate instead of pressure.

The moistening at the tropopause, below 17 km altitude, is first due to the vertical convergence of the moisture flux (Figure 2b) with a strong maximum between 5° and 30°N, extending up to 19 km (around 470 K potential temperature). This region is situated at the same latitudes as the ITCZ, characterized by deep convection producing very cold cloud tops and very low OLR (Figure 3c). Part of the strong moistening by the vertical flux is compensated by horizontal divergence, which actually reaches its largest values below 17 km as well. This is expected as the horizontal moisture flux redistributes the water vapor brought there by the vertical moisture flux. In contrast, the sink/source term (Figure 2c) leads to a dehydration between 20°S and 30°N. The sink/source term is interpreted as the tendency resulting from all processes occurring at scales finer than 0.1° (about 10 km), the resolution of the regridded output. Theses processes include from the finest to the largest scales: the microphysical processes, namely the sublimation and the condensation either by deposition or by nucleation, the turbulent mixing, and the mixing by coherent circulations finer than 0.1°. The dehydration around the tropopause is due to the condensation of the water vapor exceeding the saturation. This dehydration largely compensates the vertical convergence of the moisture flux and explains that, despite the strong maximum in the vertical moisture flux convergence, the net variation does not exhibit such a strong maximum. It matches the concept of *cold trap*, where moist air enters the stratosphere in the coldest regions where it is strongly dehydrated by freeze-drying processes (condensation). As will be shown and in line with previous studies, while the cold trap is efficient to remove water vapor around the tropopause, convection is able to bring water vapor above it.

Table 1
Contribution of the Different Budget Terms to the Simulated Net Variation of Water Vapor (in Tg), for All Points (First Line) and Over the Very Deep Convective Systems Only (Second Line)

OLR_{max}	Net variation	Hor. conv.	Vert. conv.	Sink/ source	*Input*
∞	21.3	−8.0	27.3	2.0	29.3
90	0.6	−2.6	−0.8	4.0	3.2 (11%)

Note. The budget is computed between 10°S and 30°N, between 17 and 20 km altitude, and integrated between 2 August and 8 September included. Last column is the water vapor *input* calculated as the sum of the vertical convergence and the sink/source terms. The percentage is with respect to the water vapor input for all points.

Between 17 and 20 km, the sink/source term adds water vapor. In the next section, the contribution of convection to this TLS moistening is quantified, after having demonstrated the ability of the ICON model to simulate the very deep convective systems responsible for this hydration. The pattern of the horizontal and vertical moisture flux convergence terms is more noisy but together they also contribute to the moistening of the TLS. Quantifying the contributions (see the upper row of Table 1) the sink/source term contributes 9% to the moistening of the TLS, the vertical one 128% and the horizontal one −37%. As the integral of the moisture flux convergence over the box equals the flux across the edge of the region (divergence theorem), the moistening by the vertical moisture convergence is a direct result of the upward flux at 17 km altitude, also because the vertical flux at 20 km is small in comparison. In contrast, the integral of the horizontal convergence is due to the exchanges across the region boundaries at 10°S and 30°N and indicates a net poleward export of water vapor.

5. Contribution of the Very Deep Convective Systems

The objective of this section is to isolate the contribution of the very deep convective systems to the stratospheric water vapor budget. The first step is to define a threshold, here based on OLR, to detect the very deep convective systems. Then the water vapor tendencies associated with the very deep convective systems will be explained and quantified.

5.1. Detection of the Very Deep Convective Systems

The ability of the ICON model to simulate deep convection is shown in Hohenegger et al. (2020). In particular, the simulation produces precipitation and top-of-the-atmosphere radiation fluxes averaged over −30° to 30°N and over the full simulation period that match the observed values within 8% (see Table 2 in Hohenegger et al., 2020). The center of mass of the Intertropical Convergence Zone (ITCZ) is simulated in a very good agreement with observations over both the Atlantic and Pacific oceans, although it is slightly wider (by less than 1°) than observed in 2016. The ability of ICON to simulate the deepest convection on Earth is assessed here using maps of the first percentile of the OLR time series at each grid point (a metric of the minimal OLR values). This quantity will nevertheless not be used to define the very deep convective systems, for which we rather select a fixed OLR threshold as detailed just after.

The very deep convective systems are the few deepest systems whose tops reach the lower stratosphere. These tops are overshoots. Only the systems supplied with very unstable air at the surface and internally organized so that this air experiences only little dilution by mixing with environmental air during its ascent are able to produce such overshoots into the stratosphere (Dauhut et al., 2016). Iwasaki et al. (2010) and C. Liu and Zipser (2015) documented the climatological distribution of these systems based on a combination of CloudSat satellite radar and Caliop satellite lidar observations, and on TRMM satellite radar observations, respectively. Rysman et al. (2017) characterized their microphysical profiles using the spaceborne Microwave Humidity Sounder. These systems can be identified from space thanks to their cold cloud tops, and the associated very low longwave radiation exiting the atmosphere aloft. The first percentile of the OLR time series at each grid point allows us to spot the low-OLR regions where these very deep convective systems developed, both in the CERES observation for 2016 and 2017 as well as in the ICON simulation (Figure 3). The simulated OLR first percentiles are slightly larger than the observed ones in 2016 (by 10–20 W/m^2 in the West Pacific), but in fair agreement with the observed ones in 2017. This is true over the Asian monsoon region in particular, which indicates that ICON deepest monsoon convective systems are not deeper than the observed ones. This suggests that ICON is neither producing too deep monsoon convection, which could have led to a too high injection of convective water into the stratosphere over this region. The obtained larger OLR for the 2016 comparison is consistent with the too low frequency of the lowest IR brightness temperatures as found in Senf et al. (2018), who used the same model and the same period, but integrated the model over the Tropical Atlantic only. The geographical distribution of simulated OLR is in excellent agreement with the observations from the 2 years and with the climatologies of Iwasaki et al. (2010)

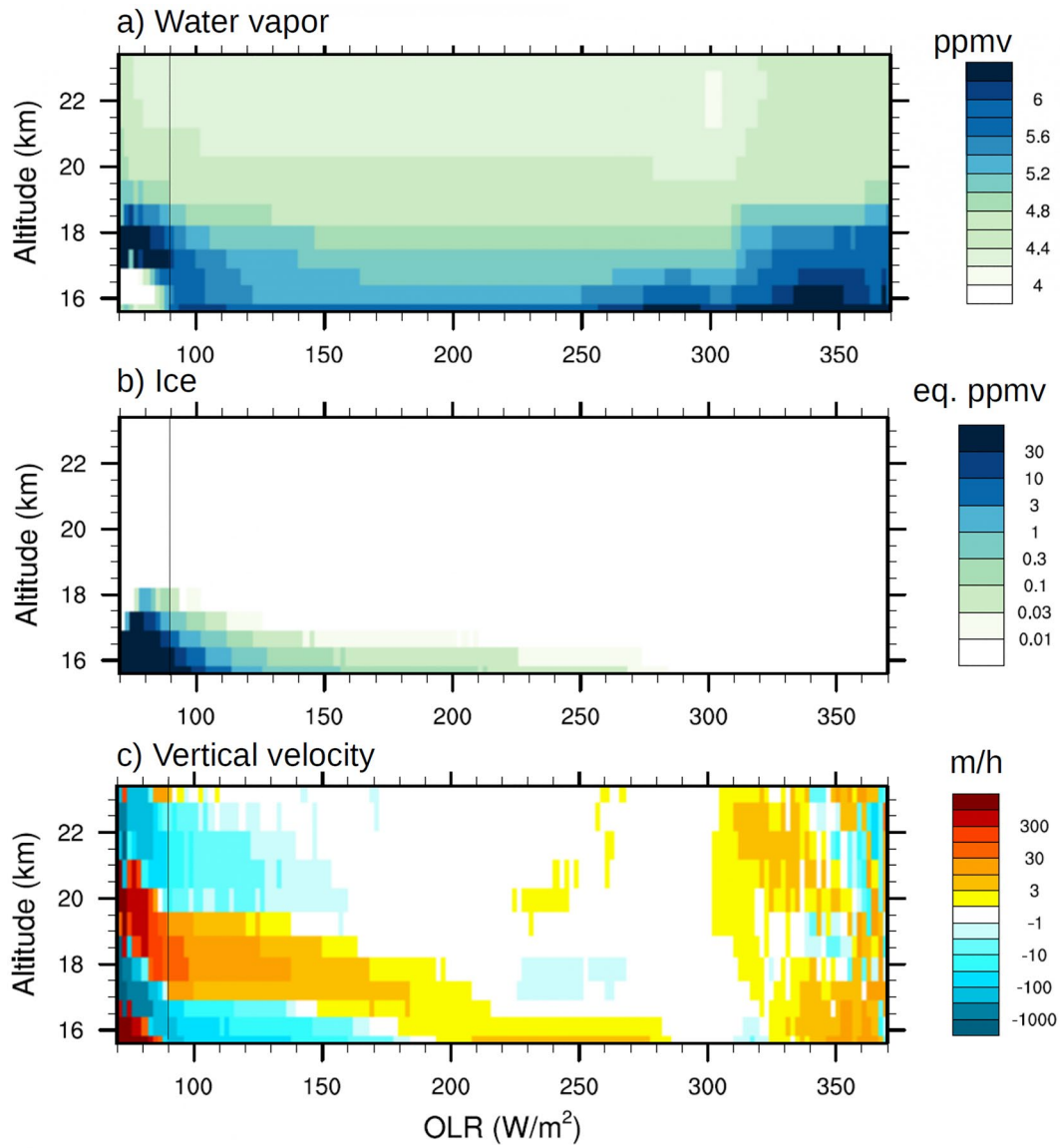

Figure 4. Conditional average of (a) water vapor volume mixing ratio, (b) ice equivalent volume mixing ratio and (c) vertical velocity as a function of altitude and OLR. The vertical line distinguishes the regions associated to the very deep convective systems, with OLR lower than 90 W/m^2, from the others.

and C. Liu and Zipser (2015). The simulation reproduces the deepest convection on Earth over the regions where it has been observed.

To define the very deep convective systems based on OLR, and to characterize them, the 4D fields of water vapor, ice and vertical velocity are conditionally averaged depending on the concomitant OLR value (Figure 4). The lower OLR regions stand out by their large stratospheric water vapor, high ice content and positive vertical velocities. This is typical of the overshoots that hydrate the stratosphere. We define here the very deep convective systems as the grid points where the ice content is larger than 1 eq.ppmv (equivalent ppmv, i.e., the same mass as 1 ppmv of water vapor) above 17 km altitude. Translating this definition to an OLR threshold, we can see in Figure 4b that this definition corresponds to regions where OLR is lower than 90 W/m^2.

At the top of the very deep convective systems, the water vapor volume mixing ratio is anomalously large with more than 6 ppmv between 17 and 18 km (Figure 4a). Just below, the air is particularly dry, with less than 4 ppmv. This is explained by the processes occurring inside the overshoots: the overshoots are extremely cold because of

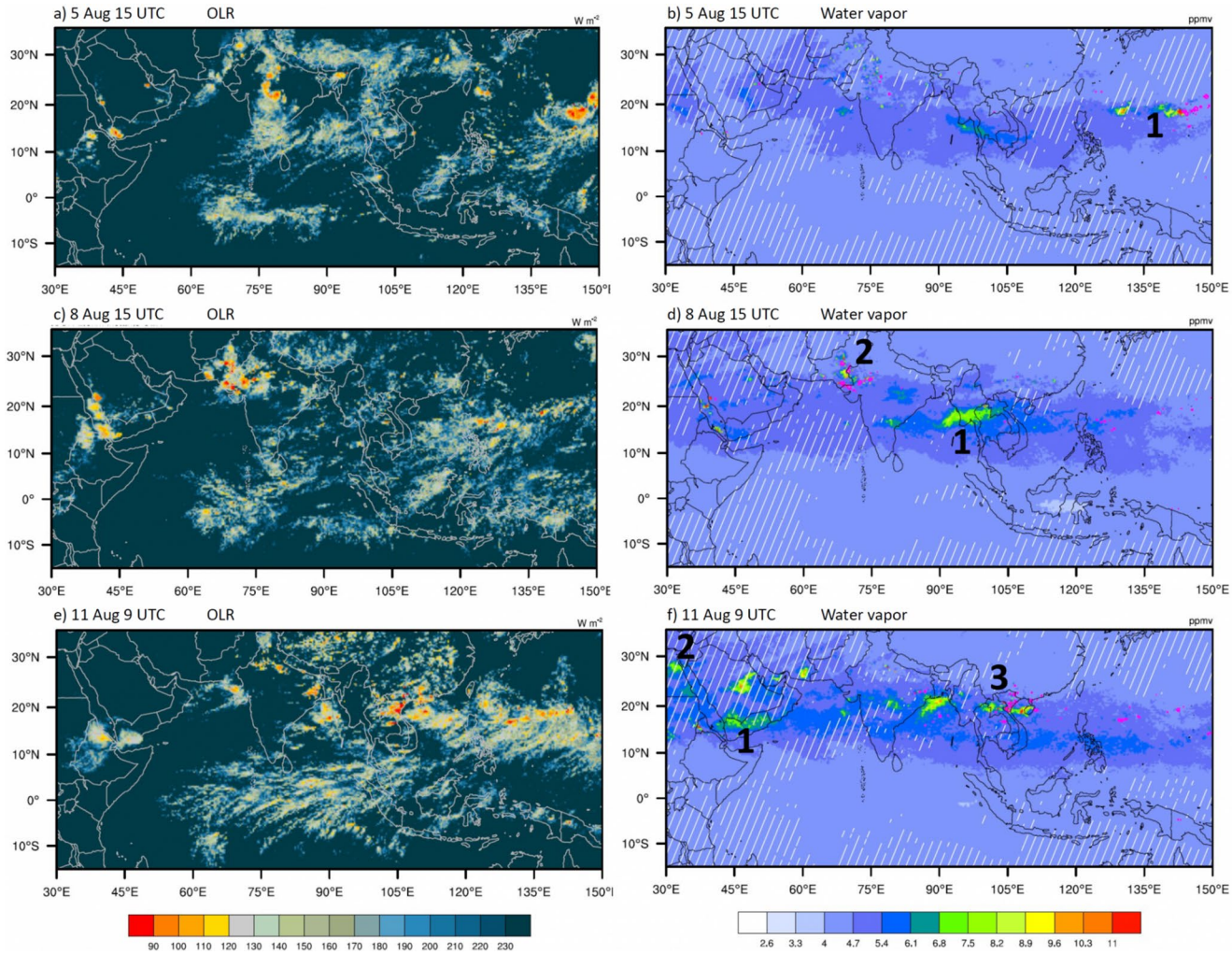

Figure 5. Distribution in ICON simulation of (left) OLR in W/m^2 and (right) water vapor volume mixing ratio in ppmv at 19-km altitude, on (a, b) 5 August at 15 UTC (c, d) 8 August at 15 UTC, and (e, f) 11 August at 9 UTC. Labels 1, 2, and 3 help to follow the hydration patches consecutive to the convective injections of water into the stratosphere. In (b, d, f), magenta thick contours delimit regions with OLR lower than 90 W/m^2 and white-hatched larger than 270 W/m^2.

the strong adiabatic cooling during their ascent. As they are colder than their environment, they are also drier, that is, they contain less water *vapor*. Most of their water content is in the ice phase. At their top, the entrainment of subsaturated stratospheric air warms the cloud, leads to intense sublimation of the ice crystals and the development of a moist anomaly (Dauhut et al., 2018). The vertical velocity at the top of the very deep convective systems (Figure 4c) is at least one order of magnitude larger than in the other regions, reaching 300 m/h on average up to 21 km.

5.2. Stratosphere Hydration by Convection

Once the very deep convective systems are detected, it is possible to visualize their impact on the stratospheric water vapor field. Figure 5 illustrates the injection of water by some very deep convective systems into the stratosphere, at 19-km altitude. Note that water vapor anomalies can be clearly seen at 19 km. As shown in Hassim and Lane (2010) and Lee et al. (2019), the water vapor anomalies lie at higher altitudes than the overshooting tops, typically 0.5 up to 1.5 km above because of top entrainment of stratospheric air (Dauhut et al., 2018) or hydraulic jump (O'Neill et al., 2021). Also individual overshoot reaching as high as 19 km do exist (e.g., C. Liu & Zipser, 2015), although they are extremely infrequent. In Figure 5 the propagation of the hydration patches injected by the very deep convective systems over the West Pacific on 5 August (labeled 1), over the border region between Pakistan and India on 8 August (labeled 2), and over Halong Bay and Hainan coasts on 11 August

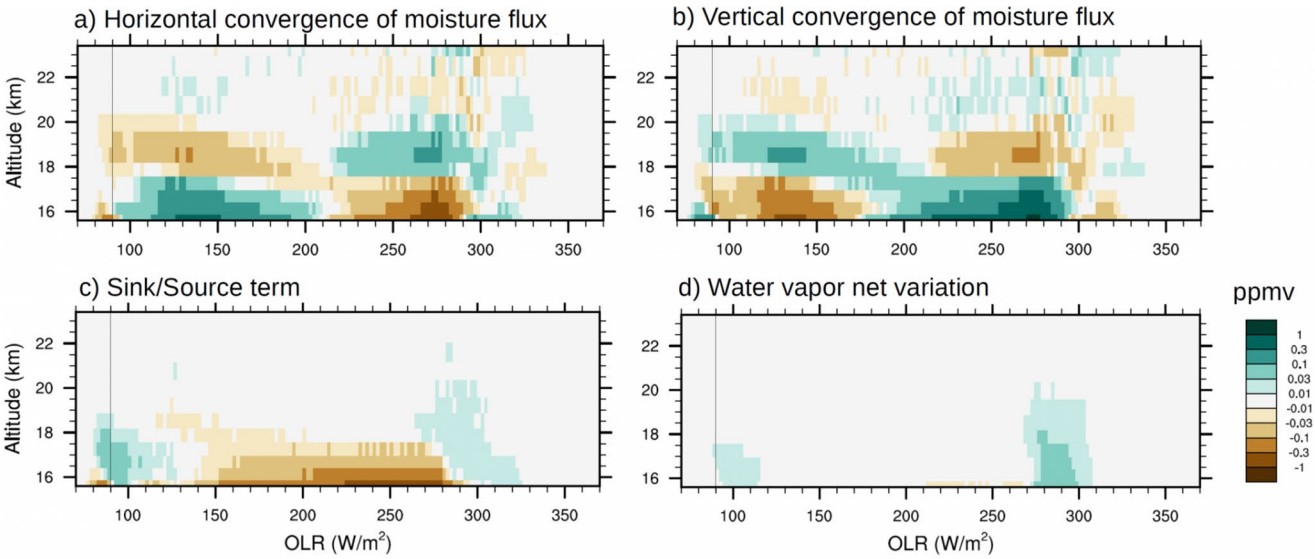

Figure 6. Contribution of the OLR bins to the budget terms of Equation 1 as a function of the altitude, integrated over the period from 02 August to 08 September and averaged over the latitudinal band between 10°S and 30°N: (a) horizontal convergence of moisture flux, (b) vertical convergence of moisture flux, (c) sink/source term, and (d) water vapor net variation. The vertical line distinguishes the regions associated to the very deep convective systems, with OLR lower than 90 W/m^2, from the others. Note that in contrast to Figure 4 that shows bin averages, here bin contributions are shown, weighting each bin by its frequency (cf. Figure S3 in Supporting Information S1). Values are in ppmv.

(labeled 3), can be visually tracked. The strong easterlies in the low stratosphere quickly advect the hydration patches away from their genesis location, over large-OLR regions. Diffusion by turbulence, itself fostered by the vertical shear of the horizontal wind, decreases the water vapor volume mixing ratio of the hydration patches, from more than 11 ppmv shortly after the injection to about 8 ppmv 3 days after. Similar advection and decrease of the water vapor anomalies shortly after the injection were already reported by Dauhut et al. (2015) and Lee et al. (2019).

5.3. Contribution to the Water Vapor Budget

Summing up the previous results, ICON produces water vapor variations in line with the observations of boreal summer (Figure 1), its TTL vertical velocities are consistent with the ones reported in this region (Figure 2), the model produces the deepest convection where it is observed (Figure 3), it produces overshoot cloud tops and the associated dry and moist anomalies in line with previous studies (Figure 4) and finally the moist patches produced downstream of the overshoot injections are as expected (Figure 5). In short, the ICON model is able to reproduce the key phenomena at play, as well as their overall impact. We can thus now assess the contribution of convection to the water vapor budget based on this ICON simulation.

By integrating the terms of the water vapor budget over all time steps, between 10°S and 30°N, and plotting them as a function of OLR, it is possible to disentangle the contribution of the different OLR regions to the stratospheric water budget (Figure 6). Here the focus is on the very deep convective systems, defined above as the regions with OLR lower than 90 W/m^2. The OLR coordinate in Figure 6 is used to primarily distinguish these very deep convective systems from the other regions, but it should not be read as a proxy for the horizontal distance from the overshooting tops. As illustrated in Figure 5, intermediate OLR values like 110–180 W/m^2 can also correspond to regions far away from the very deep convective systems. Figure 6 indicates that, in contrast to the bin averages shown in Figure 4, the few points at very low OLR contribute significantly to the different budget terms, despite their much lower frequency (cf. Figure S3 in Supporting Information S1).

The very deep convective systems do not lead to an obvious moistening (Figure 6d). In the stratosphere above them, the hydration by microphysics and subgrid-scale transport up to 19 km (Figure 6c) is compensated by the vertical moisture flux (Figure 6b) that transports part of this hydration upward, between 18 and 20 km. No net hydration is visible in these regions because of the efficient transport out of the very deep convective regions

by the divergent horizontal moisture flux (Figure 6a): this corresponds to the fast advection and spread of the hydration patches by the stratospheric winds, visible in Figure 5. In contrast, in regions with slightly larger OLR, between 90 and 110 W/m^2, a net moistening is visible and can be explained by the convergence of the horizontal moisture flux.

Table 1 summarizes the contribution of the very deep convective systems (OLR lower than 90 W/m^2) to the net moistening of the TLS. The net water vapor mass variation above the very deep convective systems corresponds to an increase of +0.57 Tg of water vapor, that is, around 3% of the water vapor mass increase in the whole TLS. The sink/source term actually adds 4.0 Tg of water vapor. The reason why most of the hydration by the sink/source term does not translate into a net increase of water vapor comes from the strong horizontal divergence of the moisture flux above the very deep convective systems that contribute to −2.6 Tg.

In order to differentiate the impact of convection itself from the impact of the diverging stratospheric winds (advection and spread of the hydration patches), we define here the stratospheric water vapor *input* as the sum of the vertical moisture flux convergence term and the sink/source term. Comparing the input of +3.2 Tg in the regions with OLR lower than 90 W/m^2, attributed to the very deep convective systems, to the input over the full TLS gives a 11% contribution of the very deep convective systems to the input of water vapor into the stratosphere.

At large OLR, the net moistening between 17 and 20 km visible in Figure 6d is due to the horizontal convergence of water vapor and the sink/source term (Figures 6a and 6c). The contribution of microphysics to this latter term is expected to be small, as the ice concentrations are very low in this range of OLR values, cf. Figure 4b. The moistening of these regions are thus due to the horizontal transport by the flow and the subgrid-scale transport including the turbulent fluxes. The spread of the hydration patches—visible in Figure 5, Figure 2 of Dauhut et al. (2015) and Figures 4 and 6 of Lee et al. (2019)—is an illustration of such transport that can occur thousands of kilometers away from the very deep convective systems, over regions with large OLR (white-hatched areas in Figure 5). This moistening by the horizontal moisture fluxes and the sink/source term is partly compensated by the vertical moisture flux that is divergent there (Figure 6b).

6. Discussion

The decomposition of the water vapor budget in the TLS and the integration of its terms over the very deep convective systems allowed us to quantify the contribution of convection to the water vapor input in the TLS. Our result, a 11% contribution, lies in the range of the estimates by previous studies. It is lower than the estimate of 18% made by Dauhut et al. (2015), who upscaled the stratospheric water vapor input from one very deep convective system. It is however not as low as the last estimate of Schoeberl et al. (2018) of 2%. The latter is computed for boreal winter, and as the difference in the stratospheric humidity between Lagrangian simulations considering and not considering the transport of water by convection. Using this method, Ueyama et al. (2015) and Ueyama et al. (2018) computed the convective contribution to the water vapor at the very specific 100 hPa level. Their estimates of 14% and 15% for boreal winter and summer, respectively, are slightly larger than our estimate.

The differences between the estimates can result from differences in: (a) the time period considered, (b) the level considered, (c) the methods used to get the estimate, and (d) the models used. The different time periods considered could explain that the estimate in Schoeberl et al. (2018) is lower than in our study. They considered a boreal winter period. Given the compilation of observations by C. Liu and Zipser (2005), the climatological abundance of overshooting convection during the month of August, investigated here, is larger than during boreal winter, but certainly not by a factor of more than 5 that would be needed to reconcile the estimates. Also, the two estimates from Ueyama et al. (2015) and Ueyama et al. (2018) suggest a very limited seasonal variation of the convective contribution to the low-stratospheric water vapor, with the caveat that these latter two estimates are based on short time periods (7 days). Especially for the comparison to the Ueyama et al. (2015) and Ueyama et al. (2018) estimates, the different levels considered could be a plausible explanation as they only considered the 100 hPa level. However, as stated in the introduction, considering only the 100 hPa should bias the estimate low, not high, as found here with our estimate. Furthermore, Ueyama et al. (2015) and Ueyama et al. (2018) ran diabatic back trajectories to convection, using monthly averaged heating rates inconsistent with the wind fields. Finally, about one third of their back trajectories end up in the stratosphere, where they set them to MLS water vapor values. This implicitly ties their results to MLS, so uncertainty remains

about the ability of their simulation to quantify the water vapor variations. This suggests that the different methods used to get the estimates might explain much of the differences as, in contrast to these other studies, we computed here a full budget of water vapor in the low stratosphere. Precisely isolating the reason for the differences between the various estimates is beyond the scope of this study and would require an international concentrated effort, for example, defining an experiment where the hydration would be computed using the different methods on the same field/time period. Finally, the differences in the model used, and especially in their representation of the microphysics, is also crucial. A way to evaluate this uncertainty would be to apply our analysis to the other storm-resolving models participating in the DYAMOND intercomparison project, something left for future work.

Besides the representation of microphysical processes, there are other sources of uncertainties associated to our results. As mentioned in Section 2, whereas the horizontal grid spacing of 2.5 km may lead to underestimate the convective injection of water vapor into the stratosphere (Dauhut et al., 2015), the use of a vertical grid spacing of 600 m may lead to an over- or underestimation of the convective hydration of the stratosphere. Also, the convective contribution of the water vapor input into the stratosphere is deduced from the sink/source term of the water vapor budget (Equation 1), a term that is computed as a residue. Using in-line budget of the condensation/sublimation processes would provide a more direct quantification. Finally further uncertainties arise due to the shortness of the simulated period. Doing similar quantification with other GSRM and using longer simulations, simulations that now become available, would help reduce such uncertainties.

Our analysis also draws to the attention the fact that deducing the convective contribution to the water transport into the stratosphere from the anomalies of humidity observed above the tropical very deep convective systems (like the ones in Figure 5) can be misleading. Indeed, whereas the local humidity increases at the top of the very deep convective systems correspond to +0.6 Tg in the simulation, that is, 3% of the water mass increase in the full TLS (Table 1), the budget indicates that this does not reflect the 11% contribution of convection to the water mass input. The difference is primarily due to the horizontal moisture fluxes, which efficiently advect the water vapor anomalies out of the very deep convective systems (Table 1 and Figure 5). This strong ventilation contrasts with the paradigm of containment, that holds at the scale of the Asian monsoon anticyclone, that is, at much larger scale than the typical size of the moist anomalies due to individual convective injections (about 100-km wide). The strong ventilation explains why a relatively limited increase of water vapor (less than +8 ppmv) is found in the stratosphere over the individual tropical very deep convective systems, as underlined in E. J. Jensen et al. (2020).

7. Conclusions

We used a simulation of the global atmosphere performed with the ICON model at a grid spacing of 2.5 km to assess the contribution of deep convection to the water vapor budget of the lower stratosphere. For the first time, global estimates of this contribution can be made without having to rely on a convective parameterization or using a trajectory model. The considered period lasts 40 days, from 1 August to 9 September 2016. The simulation reproduces the structure of the zonal and temporal average of the water vapor field. It reproduces as well the moistening of the stratosphere observed over the simulated period, with a too large amplitude compared to the observations in 2016, but in better agreement with observations from other years like 2017.

We quantified the budget of the water vapor in the TLS and disentangled its different contributions. The main source of hydration comes from the vertical fluxes of water vapor that converge up to 19 km altitude, with a net maximum localized above the ITCZ between 5° and 30°N. The hydration due to these vertical moisture fluxes is compensated locally by the horizontal moisture fluxes that redistribute the humidity southwards and northwards. Finally, the sink/source term due to the microphysics and mixing by the smaller-scale circulations subtracts water vapor from the tropopause up to 17.5 km and adds water vapor above, spreading the hydration vertically up to 20 km. For the TLS and for the simulated period, this translates into an increase of +27.3 Tg water vapor by the vertical moisture fluxes, −8.0 Tg by the horizontal ones and +2.0 Tg by the sink/source term.

To quantify the contribution of the very deep convective systems to this hydration we first identified them by their associated very low OLR. Their distribution is in excellent agreement with observations. The lowest OLR regions, with OLR lower than 90 W/m^2, exhibit typical characteristics of very deep convective systems that

overshoot into the stratosphere: significant ice content (larger than 1 eq. ppmv) and a positive water vapor anomaly (larger than 6 ppmv) above the tropopause. The computation of the water vapor budget based on the ICON simulation indicates a 11% contribution of the very deep convective systems to the water vapor input into the stratosphere. This water vapor input includes both the direct hydration by the overshoots (i.e., the sink/source term) and the vertical convergence term. The seasonal and interannual variability of this estimate remains to be investigated as well as the sensitivity of our results to the representation of the microphysical processes. 81% of the water vapor input by the very deep convective systems is directly transported away from these systems by the horizontal moisture fluxes, decreasing the amplitude of the stratospheric water vapor anomalies. Our results underline that, despite the relatively small increase of stratospheric water vapor concentration observed above the tropical very deep convective systems a full-budget computation greatly helps to quantify the contribution of convection to the stratospheric water vapor input.

Data Availability Statement

The Aura-MLS data are archived online (https://mls.jpl.nasa.gov/). The CERES SYN1deg product is available on the CERES data portal (https://ceres.larc.nasa.gov/data/). Model output supporting the conclusions of this article are archived by the German Climate Computing Centre (DKRZ) and made available through the ESiWACE project webpage (https://www.esiwace.eu/services/dyamond). The scripts for the analysis will be available online (http://hdl.handle.net/21.11116/0000-0007-989A-0) upon publication.

Acknowledgments
The authors would like to thank Hauke Schmidt, Clarissa Kroll, and Stephanie Evan for the interesting discussions about the results. They also thank the anonymous reviewers for their comments. This research was supported by the Alexander von Humboldt foundation. Open access funding enabled and organized by Projekt DEAL.

References

Baldauf, M., Seifert, A., Förstner, J., Majewski, D., Raschendorfer, M., & Reinhardt, T. (2011). Operational convective-scale numerical weather prediction with the COSMO model: Description and sensitivities. *Monthly Weather Review*, *139*(12), 3887–3905. https://doi.org/10.1175/MWR-D-10-05013.1

Banerjee, A., Chiodo, G., Previdi, M., Ponater, M., Conley, A. J., & Polvani, L. M. (2019). Stratospheric water vapor: An important climate feedback. *Climate Dynamics*, *53*(3), 1697–1710. https://doi.org/10.1007/s00382-019-04721-4

Bedka, K., Brunner, J., Dworak, R., Feltz, W., Otkin, J., & Greenwald, T. (2010). Objective satellite-based detection of overshooting tops using infrared window channel brightness temperature gradients. *Journal of Applied Meteorology and Climatology*, *49*(2), 181–202. https://doi.org/10.1175/2009jamc2286.1

Brasseur, G. P., & Solomon, S. (2006). *Aeronomy of the middle atmosphere: Chemistry and physics of the stratosphere and mesosphere* (Vol. 32). Springer Science & Business Media.

Butchart, N. (2014). The brewer-dobson circulation. *Reviews of Geophysics*, *52*(2), 157–184. https://doi.org/10.1002/2013rg000448

Corti, T., Luo, B. P., de Reus, M., Brunner, D., Cairo, F., Mahoney, M. J., et al. (2008). Unprecedented evidence for deep convection hydrating the tropical stratosphere. *Geophysical Research Letters*, *35*(10). https://doi.org/10.1029/2008GL033641

Dauhut, T., Chaboureau, J.-P., Escobar, J., & Mascart, P. (2015). Large-eddy simulations of Hector the convector making the stratosphere wetter. *Atmospheric Science Letters*, *16*(2), 135–140. https://doi.org/10.1002/asl2.534

Dauhut, T., Chaboureau, J.-P., Escobar, J., & Mascart, P. (2016). Giga-LES of Hector the Convector and its two tallest updrafts up to the stratosphere. *Journal of the Atmospheric Sciences*, *73*(12), 5041–5060. https://doi.org/10.1175/JAS-D-16-0083.1

Dauhut, T., Chaboureau, J.-P., Haynes, P. H., & Lane, T. P. (2018). The mechanisms leading to a stratospheric hydration by overshooting convection. *Journal of the Atmospheric Sciences*, *75*(12), 4383–4398. https://doi.org/10.1175/JAS-D-18-0176.1

Dessler, A. E., Schoeberl, M. R., Wang, T., Davis, S. M., & Rosenlof, K. H. (2013). Stratospheric water vapor feedback. *Proceedings of the National Academy of Sciences*, *110*(45), 18087–18091. https://doi.org/10.1073/pnas.1310344110

Doelling, D. R., Sun, M., Nguyen, L. T., Nordeen, M. L., Haney, C. O., Keyes, D. F., & Mlynczak, P. E. (2016). Advances in geostationary-derived longwave fluxes for the CERES synoptic (syn1deg) product. *Journal of Atmospheric and Oceanic Technology*, *33*(3), 503–521. https://doi.org/10.1175/jtech-d-15-0147.1

Eyring, V., Butchart, N., Waugh, D. W., Akiyoshi, H., Austin, J., Bekki, S., et al. (2006). Assessment of temperature, trace species, and ozone in chemistry-climate model simulations of the recent past. *Journal of Geophysical Research*, *111*(D22), D22308. https://doi.org/10.1029/2006JD007327

Forster, P. M. D. F., & Shine, K. P. (2002). Assessing the climate impact of trends in stratospheric water vapor. *Geophysical Research Letters*, *29*(6), 10–11. https://doi.org/10.1029/2001GL013909

Fueglistaler, S., Dessler, A. E., Dunkerton, T. J., Folkins, I., Fu, Q., & Mote, P. W. (2009). Tropical tropopause layer. *Reviews of Geophysics*, *47*(1), RG1004. https://doi.org/10.1029/2008RG000267

Hardiman, S. C., Boutle, I. A., Bushell, A. C., Butchart, N., Cullen, M. J. P., Field, P. R., et al. (2015). Processes controlling tropical tropopause temperature and stratospheric water vapor in climate models. *Journal of Climate*, *28*(16), 6516–6535. https://doi.org/10.1175/JCLI-D-15-0075.1

Hassim, M. E. E., & Lane, T. P. (2010). A model study on the influence of overshooting convection on TTL water vapour. *Atmospheric Chemistry and Physics*, *10*(20), 9833–9849. https://doi.org/10.5194/acp-10-9833-2010

Hohenegger, C., Kornblueh, L., Klocke, D., Becker, T., Cioni, G., Engels, J. F., et al. (2020). Climate statistics in global simulations of the atmosphere, from 80 to 2.5 km grid spacing. *Journal of the Meteorological Society of Japan. Ser. II*. https://doi.org/10.2151/jmsj.2020-005

Iwasaki, S., Shibata, T., Nakamoto, J., Okamoto, H., Ishimoto, H., & Kubota, H. (2010). Characteristics of deep convection measured by using the A-train constellation. *Journal of Geophysical Research*, *115*(D6), D06207. https://doi.org/10.1029/2009JD013000

Jensen, E., & Pfister, L. (2004). Transport and freeze-drying in the tropical tropopause layer. *Journal of Geophysical Research*, *109*(D2), D02207. https://doi.org/10.1029/2003JD004022

Jensen, E. J., Diskin, G., Lawson, R. P., Lance, S., Bui, T. P., Hlavka, D., et al. (2013). Ice nucleation and dehydration in the tropical tropopause layer. *Proceedings of the National Academy of Sciences*, *110*(6), 2041–2046. https://doi.org/10.1073/pnas.1217104110

Jensen, E. J., Pan, L. L., Honomichl, S., Diskin, G. S., Krämer, M., Spelten, N., et al. (2020). Assessment of observational evidence for direct convective hydration of the lower stratosphere. *Journal of Geophysical Research: Atmospheres*, *125*(15). https://doi.org/10.1029/2020JD032793

Khaykin, S., Pommereau, J.-P., Korshunov, L., Yushkov, V., Nielsen, J., Larsen, N., et al. (2009). Hydration of the lower stratosphere by ice crystal geysers over land convective systems. *Atmospheric Chemistry and Physics*, *9*(6), 2275–2287. https://doi.org/10.5194/acp-9-2275-2009

Lee, K.-O., Dauhut, T., Chaboureau, J.-P., Khaykin, S., Krämer, M., & Rolf, C. (2019). Convective hydration in the tropical tropopause layer during the StratoClim aircraft campaign: Pathway of an observed hydration patch. *Atmospheric Chemistry and Physics*, *19*(18), 11803–11820. https://doi.org/10.5194/acp-19-11803-2019

Liu, C., & Zipser, E. J. (2005). Global distribution of convection penetrating the tropical tropopause. *Journal of Geophysical Research*, *110*(D23). https://doi.org/10.1029/2005jd006063

Liu, C., & Zipser, E. J. (2015). The global distribution of largest, deepest, and most intense precipitation systems. *Geophysical Research Letters*, *42*(9), 3591–3595. https://doi.org/10.1002/2015GL063776

Liu, X. M., Rivière, E. D., Marécal, V., Durry, G., Hamdouni, A., Arteta, J., & Khaykin, S. (2010). Stratospheric water vapour budget and convection overshooting the tropopause: Modelling study from SCOUT-AMMA. *Atmospheric Chemistry and Physics*, *10*(17), 8267–8286. https://doi.org/10.5194/acp-10-8267-2010

Livesey, N. J., Read, W. G., Wagner, P. A., Froidevaux, L., Lambert, A., Manney, G. L., et al. (2017). *Earth observing system, aura microwave limb sounder (mls): Version 4.2 x level 2 data quality and description document (Tech. Rep.). Technical report*. Jet Propulsion Laboratory. D-33509.

Mlawer, E. J., & Clough, S. A. (1998). Shortwave and longwave enhancements in the Rapid Radiative Transfer Model. *Proceedings of the 7th atmospheric radiation measurement (arm) science team meeting*, 409–413.

Mlawer, E. J., Taubman, S. J., Brown, P. D., Iacono, M. J., & Clough, S. A. (1997). Radiative transfer for inhomogeneous atmospheres: RRTM, a validated correlated-k model for the longwave. *Journal of Geophysical Research*, *102*(D14), 16663–16682. https://doi.org/10.1029/97JD00237

Mote, P. W. (1995). The annual cycle of stratospheric water vapor in a General Circulation Model. *Journal of Geophysical Research*, *100*(D4), 7363–7379. https://doi.org/10.1029/94JD03301

O'Neill, M. E., Orf, L., Heymsfield, G. M., & Halbert, K. (2021). Hydraulic jump dynamics above supercell thunderstorms. *Science*, *373*(6560), 1248–1251.

Ploeger, F., Günther, G., Konopka, P., Fueglistaler, S., Müller, R., Hoppe, C., et al. (2013). Horizontal water vapor transport in the lower stratosphere from subtropics to high latitudes during boreal Summer. *Journal of Geophysical Research: Atmospheres*, *118*(14), 8111–8127. https://doi.org/10.1002/jgrd.50636 Retrieved from https://agupubs.onlinelibrary.wiley.com/doi/abs/10.1002/jgrd.50636

Randel, W. J., & Jensen, E. J. (2013). Physical processes in the tropical tropopause layer and their roles in a changing climate. *Nature Geoscience*, *6*(3), 169–176. https://doi.org/10.1038/ngeo1733

Raschendorfer, M. (2001). The new turbulence parameterization of LM. *COSMO Newsl*, *1*, 89–97.

Reinert, D. (2020). The tracer transport module Part I: A mass consistent finite volume Approach with fractional steps. *Reports on ICON*(5), 1–19. https://doi.org/10.5676/DWD_pub/nwv/icon_005

Revell, L. E., Stenke, A., Rozanov, E., Ball, W., Lossow, S., & Peter, T. (2016). The role of methane in projections of 21st century stratospheric water vapour. *Atmospheric Chemistry and Physics*, *16*(20), 13067–13080. https://doi.org/10.5194/acp-16-13067-2016

Rysman, J.-F., Claud, C., & Delanoe, J. (2017). Monitoring deep convection and convective overshooting from 60 S to 60 N using MHS: A cloudsat/CALIPSO-based assessment. IEEE geosci. *Remote Sensing Letters*, *14*(2), 159–163. https://doi.org/10.1109/LGRS.2016.2631725

Schoeberl, M. R., Dessler, A. E., Wang, T., Avery, M. A., & Jensen, E. J. (2014). Cloud formation, convection, and stratospheric dehydration. *Earth and Space Science*, *1*(1), 1–17. https://doi.org/10.1002/2014EA000014

Schoeberl, M. R., Jensen, E. J., Pfister, L., Ueyama, R., Avery, M., & Dessler, A. E. (2018). Convective hydration of the upper troposphere and lower stratosphere. *Journal of Geophysical Research: Atmospheres*, *123*(9), 4583–4593. https://doi.org/10.1029/2018JD028286

Senf, F., Klocke, D., & Brueck, M. (2018). Size-resolved evaluation of simulated deep tropical convection. *Monthly Weather Review*, *146*(7), 2161–2182. https://doi.org/10.1175/mwr-d-17-0378.1

Shindell, D. T. (2001). Climate and ozone response to increased stratospheric water vapor. *Geophysical Research Letters*, *28*(8), 1551–1554. https://doi.org/10.1029/1999GL011197

Smith, J. B. (2021). Convective hydration of the stratosphere. *Science*, *373*(6560), 1194–1195. https://doi.org/10.1126/science.abl8740

Sohn, B.-J., Ham, S.-H., & Yang, P. (2009). Possibility of the visible-channel calibration using deep convective clouds overshooting the TTL. *Journal of Applied Meteorology and Climatology*, *48*(11), 2271–2283. https://doi.org/10.1175/2009jamc2197.1

Solomon, S., Rosenlof, K. H., Portmann, R. W., Daniel, J. S., Davis, S. M., Sanford, T. J., & Plattner, G.-K. (2010). Contributions of stratospheric water vapor to decadal changes in the rate of global warming. *Science*, *327*(5970), 1219–1223. https://doi.org/10.1126/science.1182488

Stenke, A., & Grewe, V. (2005). Simulation of stratospheric water vapor trends: Impact on stratospheric ozone chemistry. *Atmospheric Chemistry and Physics*, *5*(5), 1257–1272. https://doi.org/10.5194/acp-5-1257-2005

Stenke, A., Grewe, V., & Ponater, M. (2008). Lagrangian transport of water vapor and cloud water in the ECHAM4 GCM and its impact on the cold bias. *Climate Dynamics*, *31*(5), 491–506. https://doi.org/10.1007/s00382-007-0347-5

Stevens, B. (2013). Water in the atmosphere. *Physics Today*, *66*(6), 29. https://doi.org/10.1063/pt.3.2009

Stevens, B., Satoh, M., Auger, L., Biercamp, J., Bretherton, C. S., Chen, X., et al. (2019). DYAMOND: The DYnamics of the atmospheric general circulation modeled on non-hydrostatic domains. *Progress in Earth and Planetary Science*, *6*(1), 61. https://doi.org/10.1186/s40645-019-0304-z

Ueyama, R., Jensen, E. J., & Pfister, L. (2018). Convective influence on the humidity and clouds in the tropical tropopause layer during boreal Summer. *Journal of Geophysical Research: Atmospheres*, *123*(14), 7576–7593. https://doi.org/10.1029/2018JD028674

Ueyama, R., Jensen, E. J., Pfister, L., & Kim, J. (2015). Dynamical, convective, and microphysical control on wintertime distributions of water vapor and clouds in the tropical tropopause layer. *Journal of Geophysical Research: Atmospheres*, *120*(1910), 483500–483510. https://doi.org/10.1002/2015JD023318

Waters, J. W., Froidevaux, L., Harwood, R. S., Jarnot, R. F., Pickett, H. M., Read, W. G., et al. (2006). The Earth Observing System Microwave Limb Sounder (EOS MLS) on the Aura satellite. *IEEE Transactions on Geoscience and Remote Sensing*, *44*(5), 1075–1092. https://doi.org/10.1109/TGRS.2006.873771

Wielicki, B. A., Barkstrom, B. R., Harrison, E. F., Lee, R. B., III, Smith, G. L., & Cooper, J. E. (1996). Clouds and the Earth's Radiant Energy System (CERES): An earth observing system experiment. *Bulletin of the American Meteorological Society*, *77*(5), 853–868. https://doi.org/10.1175/1520-0477(1996)077<0853:catere>2.0.co;2

Woods, S., Lawson, R. P., Jensen, E., Bui, T. P., Thornberry, T., Rollins, A., et al. (2018). Microphysical properties of tropical tropopause layer cirrus. *Journal of Geophysical Research: Atmospheres*, *123*(11), 6053–6069. https://doi.org/10.1029/2017jd028068

Zängl, G., Reinert, D., Rípodas, P., & Baldauf, M. (2015). The ICON (ICOsahedral Non-hydrostatic) modelling framework of DWD and MPI-M: Description of the non-hydrostatic dynamical core. *Quarterly Journal of the Royal Meteorological Society*, *141*(687), 563–579. https://doi.org/10.1002/qj.2378